

Toward Autonomous Robotic Micro-Suturing using Optical Coherence Tomography Calibration and Path Planning

Yuan Tian¹, Mark Draelos, PhD², Gao Tang³, Ruobing Qian²,
Anthony Kuo, MD⁴, Joseph Izatt, PhD², Kris Hauser, PhD³

Abstract—Robotic automation has the potential to assist human surgeons in performing suturing tasks in microsurgery, and in order to do so a robot must be able to guide a needle with sub-millimeter precision through soft tissue. This paper presents a robotic suturing system that uses 3D optical coherence tomography (OCT) system for imaging feedback. Calibration of the robot-OCT and robot-needle transforms, wound detection, keypoint identification, and path planning are all performed automatically. The calibration method handles pose uncertainty when the needle is grasped using a variant of iterative closest points. The path planner uses the identified wound shape to calculate needle entry and exit points to yield an evenly-matched wound shape after closure. Experiments on tissue phantoms and animal tissue demonstrate that the system can pass a suture needle through wounds with 0.194 mm overall accuracy in achieving the planned entry and exit points, and over $10\times$ more precise than prior autonomous suturing robots.

I. INTRODUCTION

Suturing is a basic surgical skill used in microsurgery to repair wounds and severed blood vessels and nerves, but it is tedious, time-consuming, and requires substantial training [1]. Robotic assistance has been proposed for suturing in open surgery, laparoscopic surgery, and microsurgery, with teleoperated surgical systems increasing the surgeon's dexterity, as well as autonomous techniques that can alleviate burden on the surgeon. Automation of suturing is still a challenging task due to deformation of the tissue as the needle passes through it, the need for regrasping to complete multiple throws, and incorporation of imaging feedback to estimate wound shape and guide the needle successfully along planned paths. The needle is occluded as it passes through the tissue, and it is difficult to perform accurate 3D mapping of biological tissues with stereo vision techniques. The challenge is particularly acute in the microsurgery setting, since existing sensing and actuation technologies do not perform at the required level of precision needed to complete reliable suturing.

We achieve sub-millimeter suturing precision, and propose a needle calibration and insertion system with optical coherence tomography (OCT) imaging (Fig. 1). OCT is a laser-based imaging technique that exploits interference to

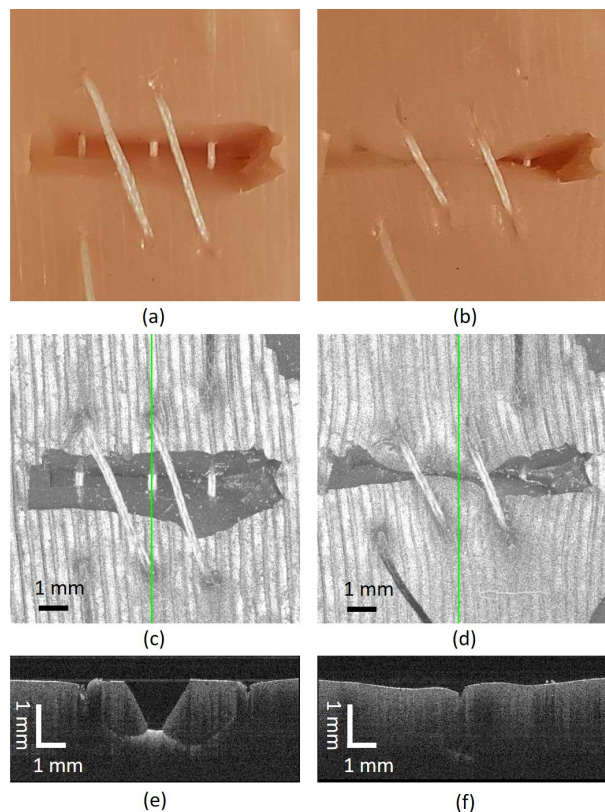


Fig. 1. A sub-centimeter multi-throw suture before (a) and after (b) closing the wound. The wound is fully approximated between the second throw's right bite point and left exit point. The OCT volume projection is shown before (c) and after (d) closing the wound. (e) The highlighted B-scan ((c)'s green line) in the OCT volume before closing the wound. (f) The B-scan after closing the wound, showing no dead space [5].

resolve the distance of reflectors along the beam's path to within several micrometers [8]. By scanning the beam, a cross-sectional view (or B-scan) of the tissue is produced, and further sweeping the beam in a raster pattern yields a 3D volume (a $\sim 1\text{cm}^3$ cube in our system). Although OCT has deepest penetration in transparent tissues like those of the eye, it can also be used to image the surfaces and first millimeters of scattering tissues like skin. OCT has also been used to track tissues and surgical tools in eye surgery [12]. To guide the needle precisely, we perform calibration, perception, and planning in the OCT imaging frame. To calibrate the needle tip and robot with respect to the OCT frame, we use the observed needle surface voxels to simultaneously optimize the needle, robot, and OCT frames

This work is partially supported by NIH Grant R21-EY029877.

¹ Y. Tian is with the Department of Electrical and Computer Engineering, Duke University, Durham, NC, USA. yuan.tian277@duke.edu

² M. Draelos, R. Qian and J. Izatt are with the Department of Biomedical Engineering, Duke University, Durham, NC, USA.

³ G. Tang and K. Hauser are with the Department of Computer Science, University of Illinois Urbana-Champaign, Urbana, IL, USA.

⁴ A. Kuo is with the Department of Ophthalmology, Duke University Medical Center, Durham, NC, USA.

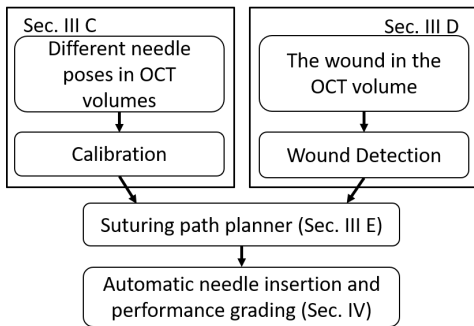


Fig. 2. The flow chart of the overall robotic suturing procedure, which can be divided into coordinates calibration, wound detection, suturing path planning, automatic needle insertion, and performance grading.

with a modified iterative closest points (ICP) [2] algorithm that emphasizes an accurate fit at the needle tip. A suturing path planner chooses a suturing path such that the two sides of the wound will match after closure, without dead space [5]. Fig. 2 shows the overall procedure for our robotic suturing process.

Closed-loop imaging guidance is challenging due to OCT artifacts including refraction and shadowing by the needle driver. Instead, our experiments observe that open-loop execution of a circular suture path leads to high accuracy between the planned and actual needle entry and exit points, even under significant tissue deformation. A unique aspect of our experiments is that we use 3D OCT to image the resulting suture path after the needle is pulled through and the tissue returns to a rest state. Experiments in a tissue phantom and porcine skin show the targeted entry and exit points are reached with root mean square error (RMSE) of 0.194 mm, which is less than half the width of the needle and over $20\times$ more precise than prior autonomous suturing robots.

II. RELATED WORK

Several researchers have studied the use of robots and imaging guidance for suturing and micromanipulation assistance. Using direct teleoperation, human surgeons are able to complete suturing for anastomoses of 3mm artificial blood vessels using the Intuitive Surgical DaVinci robot [1], but to our knowledge surgical robots have not yet been used for microsurgical suturing in vivo.

Autonomous suturing has been studied for at least two decades. Early work by Kang and Wen proposes a laparoscopic robot that can perform manually controlled or semi-autonomous motions for several tasks, including suturing and automatic knot tying [10]. Each motion is initiated by a surgeon. Staub et al. present an image-based guidance system for improved accuracy in guiding a suturing needle to pierce the tissue at a surgeon-indicated spot, as directed by a laser pointer [16]. 3–10 mm errors were observed from their system. More recent work has addressed multi-throw suturing using a dual armed laparoscopic robot, using a special needle gripper that reduces grasp positioning errors and feedback from a stereo vision system [15]. Their calibration

system obtains needle predictions with translational error of approximately 2.9mm, and completes 86% of throws. Our path planner is highly related to the method of Jackson and Cavusoglu for path planning of needles entering triangular shaped wounds [9]. The geometry of a circular needle entering a wound was analyzed, and we adopt many of the same conventions here. Their paths were executed on a DaVinci robot with a 12.7 mm radius needle. A similar approach was adopted by Pedram et al. who studied the problem of needle selection for varying wound geometries [14]. The errors of their entry and exit points were greater than 4.5 mm with a 15 mm radius needle. Overall, accuracy must be improved significantly for autonomous suturing in microsurgery. Our system integrates the planner with imaging feedback, calibration, and analysis of errors in the suture path for a needle with 4.14 mm radius, and we obtain over an order of magnitude improvement in accuracy.

In the microsurgical domain, OCT-guided robots have been studied as a method for assisting surgeons to complete telemanipulated tasks, primarily in the eye. Yu et al. present a B-mode OCT-integrated forceps tool for haptic-controlled microsurgery to assist in retinal membrane peeling [17]. Nasser et al. present an OCT and robot guidance system to assist in precise injections for macular degeneration [13]. Draelos et al. present a hand-guided robot that provides stabilization and OCT guidance in the cornea [3], which they further extend with autonomous needle insertion capabilities [4].

Our calibration process is highly related to the work of Zhou et al. that presents an OCT-based needle tip tracking and calibration scheme [18]. This work identified pixels likely to belong to the needle from the OCT B-scans and segmented the needle from the background using a voting scheme. Calibrating the robot-OCT frame and tracking the needle led to an impressive $\approx 10\mu\text{m}$ error as the needle moved along an XYZ translation stage. They also extended their method to 6 degree of freedom (DOF) tracking using ICP with similar levels of accuracy [19]. Our work differs in that we consider a curved needle grasped by a needle driver, which makes needle identification more difficult due to artifacts caused by shadowing, saturation artifacts, and mirror images from the complex conjugate of the needle driver. Furthermore, our calibration process accounts for regripping errors rather than using a fixed needle mount.

III. METHODS

Our system is designed to calibrate a robot-mounted circular needle and automatically insert it through a wound, all using OCT imaging. To focus on the calibration and path planning problems, we show only the single-throw problem and leave multi-throw suturing for future work. Our method assumes that 1) the needle body is a circular arc; 2) the needle diameter is larger than the wound width, so that no significant travel is needed to bring the wound sides together; 3) the entire wound is within the robot and OCT workspaces; and 4) the patient anatomy permits needle insertion by rotation about an axis parallel to the wound.

Consider the plane of the needle and a cross sectional view of a wound, where the needle is passing from right to left. To close the wound, the needle passes through the right bite point, right exit point, left bite point, and the left exit point in sequence (Fig. 3). If the right exit point and left bite point are not well-aligned with the wound’s deepest point, the resulting dead space after wound closure (Fig. 4) promotes infection [5]. Our planner generates a suture path that avoids such dead space.

A. Error Analysis

The overall needle guidance error is influenced by many elements:

- *Needle grasping uncertainty* is introduced when the the needle driver grasps the needle.
- *Wound calculation errors* can be introduced during wound segmentation and keypoint identification.
- *Needle and OCT calibration error* remain after calibration, although needle grasping uncertainty is reduced.
- *Robot repeatability and accuracy* limits the overall system performance.
- *Tissue deformation* from friction as the needle passes through the tissue can be significant.
- *Conjugate image overlap* in OCT can produce artifacts that cause errors in needle identification.

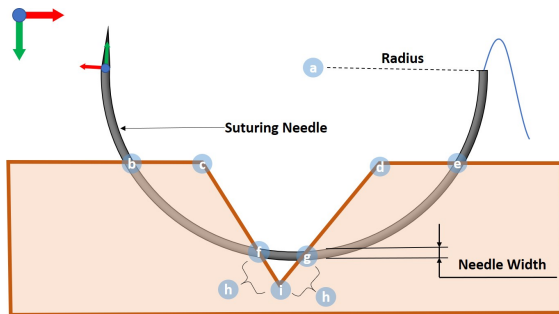


Fig. 3. Cross-sectional geometry of the incised wound and suturing path, showing a) suturing center, b) left exit point, c) wound start point, d) wound end point, e) right bite point, f) left bite point, g) right exit point, h) distance from the deepest point to the left bite point (set to be equal to the distance to the right exit point), i) wound deepest point.

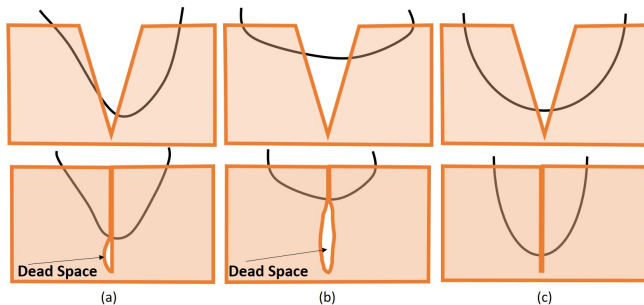


Fig. 4. (a) The left bite point is higher than the right exit point, so a dead space remains after closure. (b) The suturing depth is not sufficiently deep, which leaves a dead space after the wound is closed. (c) When the suturing path equalizes the wound sides and is sufficiently deep, then no dead space remains post-closure.

We mitigate these errors through calibration to significantly reduce the needle grasping uncertainty and surgeon supervision of wound analysis. Robot error is minimized with a repeatability of $10\ \mu\text{m}$. The overall error is thus dominated by residual calibration error and tissue deformation. Closed-loop corrections under OCT imaging feedback would further reduce this error, but mid-insertion images suffer from shadowing, saturation artifacts, and refraction.

B. Hardware

We use a custom OCT engine with a 100 kHz swept-source laser centered at 1060 nm (Axsun Technologies; Billerica, MA), an adjustable transmissive reference arm, and balanced detection. We configured this engine [3] to capture OCT volumes with sampling density $725 \times 800 \times 1327$ pixels and field of view $10 \times 10 \times 7.15$ mm. Our robot to perform the suturing needle insertion is a 6-joint IRB 120 Robot (ABB Robotics; Shanghai, China) with a specified repeatability of $10\ \mu\text{m}$.

A taper point, half-circle 4-0 suturing needle with 13 mm arc length is used for tissue phantom and porcine skin insertions. The needles’ widths, as marked in Fig. 3 is 0.448 mm. The needle is grasped with a locking Castroviejo needle driver (Ambler Surgical; Exton, PA) which is mounted to the robot’s end-effector with a custom holder. This holder keeps the grasped needle’s rotation axis approximately coincident with the robot’s last joint axis. This minimizes robot wrist and elbow movement to avoid collision with the surgical field and patient. An arbitrary view of experiment hardware is shown in Fig. 5.

C. Calibration

Our calibration procedure calculates the transformations from the world frame to the OCT frame and from the robot end-effector frame to the needle frame. We define the needle origin at the interface between the needle tip and the needle body which facilitates path planning. The needle tip’s conical nature causes the body and tip to follow separate paths when rotated [9]. This misalignment may cause friction and deformation between the needle body and the suturing path.

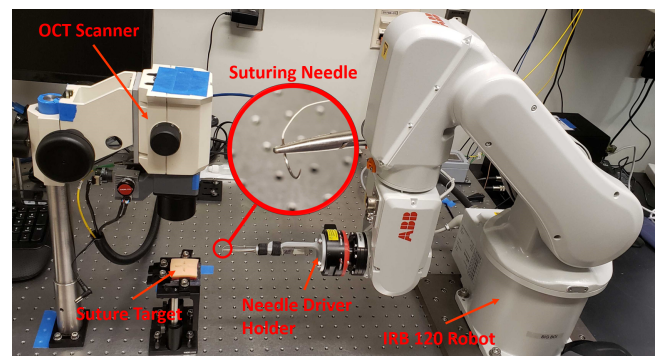


Fig. 5. An arbitrary view of the experiment hardware, including a OCT scanner, a suture target, a suturing needle, a needle driver, a needle diver holder, and an IRB 120 robot.

1) *Needle Segmentation in OCT volumes*: Our needle segmentation method is similar to [12]. We first generate the projection map of the OCT volume (Fig. 6(a)), and apply a brightness threshold to obtain a binary image. As the needle driver’s projection always appears at one side of the binary image, we clip the corresponding side of the image to remove the needle driver. We then apply the connected component algorithm [6] to find the largest connected component in the volume, which includes parts of the needle and the saturation artifacts (Fig. 6(b)). The points in the OCT volume under the connected component’s projection are the needle and the saturation artifacts’ point clouds with noise (Fig. 6(c)). We then remove the saturation artifacts in the OCT volume, which appear as straight lines that are parallel to the OCT volume’s B-scan direction and always touch or approach the edge in the OCT volume. Finally, we perform point cloud outlier removal [20] to filter out the noise below and above the needle’s point cloud (Fig. 6(d)).

2) *ICP Estimates of Needle Tip Transform*: To estimate the needle transform in the OCT frame, we use Iterative Closest Points [2] which aligns points in the OCT field (source point cloud) and the needle CAD model (target point cloud). We identify the needle points as a subset of the bright pixels in the OCT maximum intensity projection (MIP). Standard ICP frequently mismatches the needle tip, however, because the point is dominated by body points (Fig. 7(a)). We overcome this problem by estimating tip points from an initial ICP fit and increasing their weight for a second ICP fit (Fig. 7(b)). The second fit yields better alignment, especially at the needle tip.

3) *Calibration Algorithm*: We seek to solve

$$T_{ICP} = T_{OCT}^{-1} T_{EE} T_N, \quad (1)$$

where T_N is the needle frame in the end-effector frame, T_{OCT} is the OCT frame in the world, T_{EE} is the end-effector frame in the world from forward kinematics, and T_{ICP} is the ICP-derived transformation from the needle frame to the OCT frame. As described below, the robot will be guided to m different poses, yielding paired observations T_{ICP_i} and T_{EE_i} , for $i = 1, \dots, m$. We minimize the error in Eq. 1 over T_N and T_{OCT} using a Levenberg-Marquardt method.

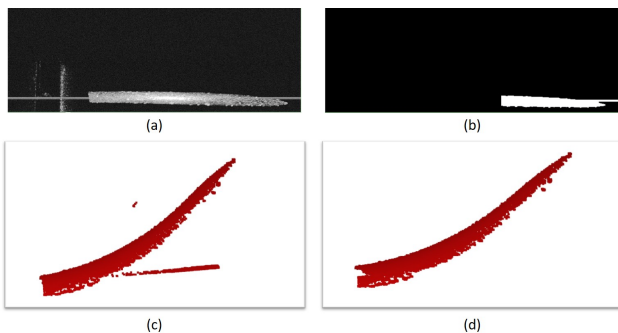


Fig. 6. (a) The clipped projection of an OCT volume during calibration. (b) The largest connected component after clipping out the needle driver. (c) The point cloud including the part of needle, the saturation artifacts, and the noise. (d) The point cloud with saturation artifacts and noise removed.

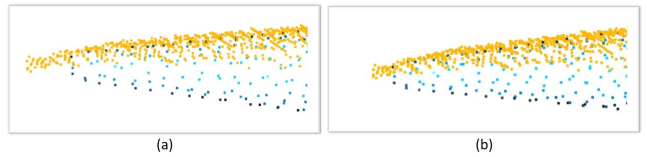


Fig. 7. The yellow point clouds are the source point clouds captured in the OCT system, and the blue point clouds are target point clouds built in the CAD software. (a) Original ICP result. We transfer the source point cloud to the target point cloud frame. The needle tip of these 2 point clouds has mismatching. (b) The modified ICP result. The mismatching of the 2 point clouds has been alleviated. (Best viewed in color)

4) *Calibration Set Sampling*: Our calibration set is an automatically defined set of $m = 9$ robot configurations. These should be chosen so that needle poses are sampled roughly uniformly across the OCT workspace and with a diversity of needle orientations. The needle tip’s point cloud must also be visible and not shadowed by the body or needle driver.

First, we manually jog the robot to move the needle tip into the center of the OCT volume. The robot then moves its end effector a small distance to produce two additional needle poses. Based on these 3 poses, we perform a rough calibration of \tilde{T}_{OCT} and \tilde{T}_N . Because these poses are near each other and the OCT volume’s center, the rough calibration is typically not sufficiently precise at the edge of the OCT frame. We thus define m desired ICP poses $T_{ICP_{des}}$ in the OCT frame such that the needle’s poses uniformly sample the field of view with different orientations. Using the below equation

$$T_{EE} = \tilde{T}_{OCT} T_{ICP_{des}}^{-1} \tilde{T}_N^{-1}, \quad (2)$$

we compute m end effector transforms, and m robot configurations are automatically generated by inverse kinematics (IK) solver [7]. Calibration is run a final time to obtain more precise estimates of T_{OCT} and T_N .

D. Wound Analysis

Wound analysis processes an OCT B-scan image and produces the following shape information: the top layer, the start point, the end point and the deepest point. We begin by using the adjusted mean arc length (AMAL) graph search method of Keller et al. [11] to find the top layer of the wound (Fig. 8(a)). Next, we rotate the top layer such that the non-wound portion is horizontal. We use a Gaussian 1D filter to denoise the top layer, and then calculate the gradient of the smoothed top layer (Fig. 8(b)). We define the start point as the first point from left to right where the gradient falls below a threshold. Similarly, we define the end point as the first point from right to left where the gradient exceeds a threshold. The point that has smallest position is the deepest point of the wound.

E. Suturing Path Planning

Once the wound is identified, we generate a suitable suturing path in the B-scan plane. We fix the suturing center to reduce the interaction forces between the needle and

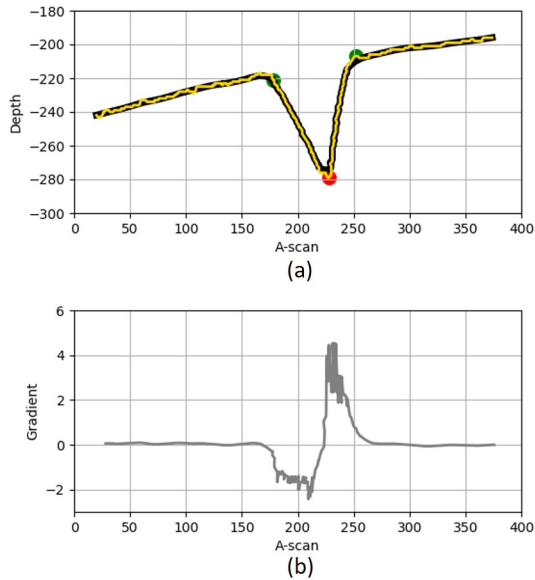


Fig. 8. Wound top layer detection and geometric analysis. (a) The AMAL detection result is shown in yellow while the de-noised result is shown in black. The estimated start and end of the wound are shown in green, while the deepest point is shown in red. (b) The gradient of the top layer of the wound after being de-noised.

tissue compared to the moving center suturing approach. To avoid the dead space (Fig. 4(a)-(b)), the distance from the left bite point to the deepest point, and the distance from the deepest point to the right exit point should be equal. According to standard suturing practice, the suturing depth should exceed 50% of the wound depth. We therefore choose a target suturing depth of 80%, from which we can calculate the left bite point and the right exit point. Using the known needle radius, we obtain two solutions for the suture center corresponding to these points in the B-scan plane. One solution lies within the tissue whereas the other is above it. We reject the in-tissue solution because its suturing path does not have the right bite point and the left exit point and use the other solution for planning.

After we obtain the suturing center in 3D, we generate the robot’s path in joint space. First, we choose three points in the needle frame (the needle tip P_{N_1} , the needle body P_{N_2} , and the needle tail P_{N_3} , every point is a 3×1 matrix). These three points determine the suturing needle position and orientation. Second, we uniformly interpolate needle tip P_{O_1} milestones along the suturing path in the OCT frame. Because the relationship between these three points is fixed, for each milestone, we calculate the corresponding P_{O_2} and P_{O_3} . Using T_{OCT} from the calibration process, we transfer the milestones from the OCT frame to the world frame (P_{W_1} , P_{W_2} and P_{W_3}). For each milestone on the suturing path, we use the relationship

$$\begin{bmatrix} P_{W_1} & P_{W_2} & P_{W_3} \\ 1 & 1 & 1 \end{bmatrix} = T_{EE} T_N \begin{bmatrix} P_{N_1} & P_{N_2} & P_{N_3} \\ 1 & 1 & 1 \end{bmatrix}. \quad (3)$$

Finally, we use the Klamp’t [7] numerical inverse kinematics solver to compute the robot configuration from the T_{EE}

of every milestone. For the first IK solution, the solver is seeded with the robot’s current configuration. For the remainder, the solver’s is seeded from the last solution. Collision detection is used to prevent the robot from colliding with the environment or itself.

IV. EXPERIMENTS AND RESULTS

A. Parameter Selection and Calibration Results

We evaluated our system in two materials: a silicone rubber tissue phantom (Your Design Medical; Brooklyn, NY) and porcine skin. Because the scope of this paper does not include needle grasping, we stopped the robot after each full insertion to detach the needle and pull the attached suture through the tract. This allows the tissue to relax to its rest deformation, although the tissue is not perfectly elastic and therefore may not relax completely. The suture path is then imaged using the OCT system.

We performed 22 suturing needle insertions (12 for tissue phantom and 10 for porcine skin). We adjusted the OCT scanner before each attempt to ensure that the wound was within its the field of view. Furthermore, in real surgical settings, the needle will be grasped at a slightly different location every time. To simulate errors caused by grasping, we grasped the needle at the different location on the jaw for each insertion, such that transformations T_{OCT} and T_N changed. Notably, the wound shape varied across all 22 insertions. The wound width was 2.493 mm – 5.110 mm whereas the wound depth was 1.643 mm – 3.082 mm. The tissue surface was also not necessarily level with tilts of $\pm 9^\circ$ to simulate the real wound environment.

For calibration, we sampled 9 robot configurations to estimate the T_{OCT} and T_N . With these 9 robot configurations, the suturing needle was uniformly sampled in the OCT space with different positions and orientations, and we estimated T_{OCT} and T_N . Comparing the difference between $T_{ICP_i}^{-1}$ and $T_{OCT}^{-1} T_{EE_i} T_N$ for our 22 groups of data, the translation RMSE

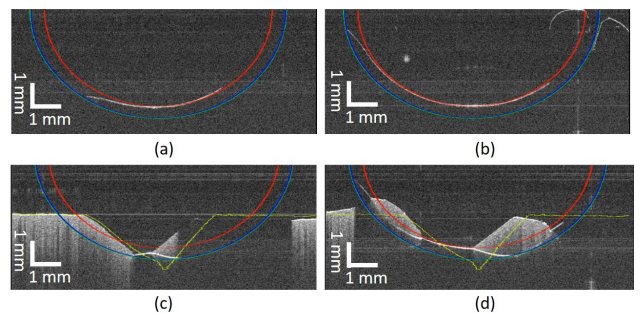


Fig. 9. Snapshots of the needle insertion process, showing the OCT B-scan data and the planned path for the needle, showing planned arcs for the inside face (red), outside face (blue), and needle tip (green, almost overlapping with the blue line). The yellow line is the wound top layer in the undeformed state. In (a) – (b), the path is executed without the tissue phantom present, showing high accuracy of the calibration process. In (c) – (d), the needle is inserted into the tissue phantom, showing significant deformation. Note that OCT cannot see the needle outside face path because the laser cannot penetrate metal. The needle shadows the tissue, and also appears distorted in the tissue due to refraction.

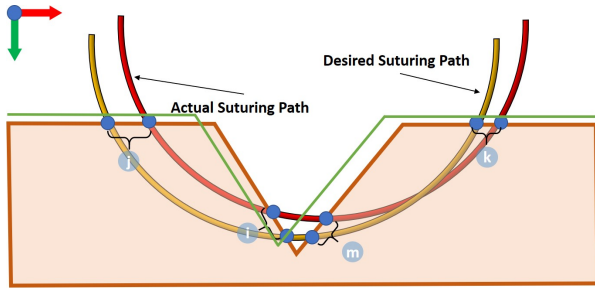


Fig. 10. The method used for suture grading. The tissue shape is after the needle pulled out, and the green line is the AMAL result before needle insertions. k) right bite point error. m) right exit point error. i) left bite point error. j) the left exit point error.

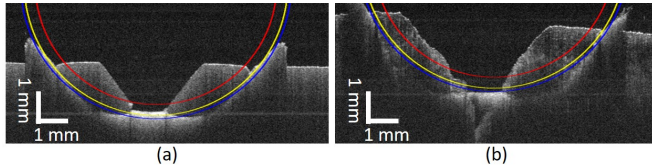


Fig. 11. OCT B-scan images of the sutures after the needle has passed through the tissue. (a) is in the tissue phantom, and (b) is porcine skin. The planned needle paths are shown for the needle inside face (red), outside face (blue), and suture top layer (yellow).

was 0.075 mm – 0.227 mm, and the rotation RMSE was 0.014 rad – 0.090 rad.

To empirically tune and evaluate wound analysis, we gathered 590 B-scans of different size wounds, and compared our method against manual grading as ground truth. With the AMAL [11] parameter $x = 1.02$, AMAL detected all wound top layers successfully. The denoising Gaussian kernel standard deviation is set to be 8 pixels, and the gradient threshold to detect the start point of the wound and the end point of the wound is chosen to be -1.5 and $+1.5$, respectively. With these values, our methods successfully detected 582 wounds and keypoints as compared to manual grading (98.6% success rate).

B. Needle Insertion Results

We first executed suturing paths in free space to visualize whether the needle follows our planned path. A representative result is shown in Fig. 9(a)-(c), demonstrating close agreement. Next, we performed insertions in the tissue phantom (Fig. 9(d)-(f)). Because it is difficult to observe the suture path with OCT when the suture passes far below the tissue surface, we graded the accuracy of insertions by calculating the distance between the planned and actual points where the suture intersects the tissue (Fig. 10). However, due to tissue deformation, it is difficult to judge whether the needle bites and exits at our planned points. Therefore, we manually removed the needle from the needle driver, and pulled the suture through the wound. Because the friction from the needle is removed and the suture is loose, the wound will approximately return to its resting shape (Fig. 11). By inspection, the sutures' paths are in the planned boundary of the needle. The RMSE for each of the four grading points for

TABLE I
TISSUE PHANTOMS SUTURE RMSE (MM, $N = 12$)

	B-scan (X)	A-scan (Y)	C-scan (Z)	3D
Right Bite	0.081	0.059	0.142	0.174
Right Exit	0.076	0.116	0.084	0.162
Left Bite	0.091	0.132	0.076	0.177
Left Exit	0.151	0.077	0.091	0.192
Total	0.104	0.100	0.102	0.177

TABLE II
PORCINE SKINS SUTURE RMSE (MM, $N = 10$)

	B-scan (X)	A-scan (Y)	C-scan (Z)	3D
Right Bite	0.077	0.053	0.106	0.141
Right Exit	0.114	0.148	0.059	0.196
Left Bite	0.061	0.167	0.084	0.197
Left Exit	0.253	0.098	0.096	0.288
Total	0.147	0.125	0.088	0.212

the tissue phantom and porcine skin are shown in Tables I and II, respectively. The RMSE for each of the grading points and overall was lower than half the width of the needle, and 0.194 mm averaged over both tissue conditions.

Our final test performed a multi-throw suturing task on the tissue phantom (Fig. 1). After each insertion, we manually unmounted the needle from the needle driver, pulled the suture through, and then re-mounted the needle for the next throw. Needle calibration was performed after each throw as usual. After three throws, we manually closed the wound by pulling on both ends of the suture. OCT images show good alignment of the wound boundary and no dead space. The problem of autonomous regrasping and wound closure in multi-throw micro-suturing is left for future work.

V. CONCLUSION

We presented a method for OCT-guided calibration and path planning for a suturing needle to be guided autonomously and accurately through soft tissue. Calibration, wound detection, and path planning are all performed using the input from OCT imaging. Execution performance was graded by the observing the path followed by the suture, demonstrating sub-millimeter errors between the planned and executed entry and exit points, with error magnitude less than half the width of the needle.

In the future, we hope to address some remaining issues in our work. First, the needle calibration error is approximately $20\times$ larger than the best-reported OCT-based calibration results in the literature, because the curved needle and needle grasping error introduce more challenging initialization and imaging conditions. More advanced image processing techniques may address OCT imaging artifacts such as highlights, refraction, shadowing, and mirror images to perform needle and wound tracking in real time. Solving these issues is a prerequisite for closed-loop guidance during suturing.

REFERENCES

- [1] T. Alrasheed, J. Liu, M. M. Hanasono, C. E. Butler, and J. C. Selber. Robotic microsurgery: Validating an assessment tool and plotting the learning curve. *Plastic and reconstructive surgery*, 134(4):794–803, 2014.
- [2] P. Besl and N. McKay. A method for registration of 3-d shapes. *IEEE Transactions on Pattern Analysis and Machine Intelligence*, 14(2), 1992.
- [3] M. Draelos, B. Keller, G. Tang, A. Kuo, K. Hauser, and J. Izatt. Real-time image-guided cooperative robotic assist device for deep anterior lamellar keratoplasty. In *IEEE International Conference on Robotics and Automation (ICRA)*, 2018.
- [4] M. Draelos, G. Tang, B. Keller, A. Kuo, K. Hauser, and J. Izatt. Optical coherence tomography guided robotic needle insertion for deep anterior lamellar keratoplasty. *IEEE Transactions on Biomedical Engineering*, 2019.
- [5] Ethicon. *Wound Closure Manual*. Ethicon Inc., 2005.
- [6] C. Grana, D. Borghesani, and R. Cucchiara. Optimized block-based connected components labeling with decision trees. *IEEE Transactions on Image Processing*, 19(6):1596–1609, 2010.
- [7] K. Hauser. Robust contact generation for robot simulation with unstructured meshes. In *International Symposium on Robotics Research*, 2013.
- [8] D. Huang, E. Swanson, C. Lin, J. Schuman, W. Stinson, W. Chang, M. Hee, T. Flotte, K. Gregory, C. Puliafito, and J. Fujimoto. Optical coherence tomography. *Science*, 254:1178–1181, 1991.
- [9] R. Jackson and M. Cavusoglu. Needle path planning for autonomous robotic surgical suturing. In *IEEE International Conference on Robotics and Automation (ICRA)*, 2013.
- [10] H. Kang and J. Wen. Autonomous suturing using minimally invasive surgical robots. In *IEEE International Conference on Control Applications*, 2000.
- [11] B. Keller, D. Cunefare, D. Grewal, T. Mahmoud, J. Izatt, and S. Farsiu. Length-adaptive graph search for automatic segmentation of pathological features in optical coherence tomography images. *Journal of Biomedical Optics*, 21(7):076015, 2016.
- [12] B. Keller, M. Draelos, G. Tang, S. Farsiu, A. Kuo, K. Hauser, and J. Izatt. Real-time corneal segmentation and 3d needle tracking in intrasurgical oct. *Biomedical Optics Express*, 9(6):2716–2732, 2018.
- [13] M. A. Nasser, M. Maier, and C. Lohmann. A targeted drug delivery platform for assisting retinal surgeons for treating age-related macular degeneration (amd). In *Int. Conf. IEEE Eng. Med. Biol. Soc. (EMBC)*, pages 4333–4338, 2017.
- [14] S. Pedram, P. Ferguson, J. Ma, E. Dutson, and J. Rosen. Autonomous suturing via surgical robot: An algorithm for optimal selection of needle diameter, shape, and path. In *IEEE International Conference on Robotics and Automation (ICRA)*, 2017.
- [15] S. Sen, A. Garg, D. G. ad S. McKinley, Y. Jen, and K. Goldberg. Automating multi-throw multilateral surgical suturing with a mechanical needle guide and sequential convex optimization. In *IEEE International Conference on Robotics and Automation (ICRA)*, 2016.
- [16] C. Staub, T. Osa, A. Knoll, and R. Bauernschmitt. Automation of tissue piercing using circular needles and vision guidance for computer aided laparoscopic surgery. In *IEEE International Conference on Robotics and Automation*, 2010.
- [17] H. Yu, J. Shen, R. Shah, N. Simaan, and K. Joos. Evaluation of microsurgical tasks with oct-guided and/or robot-assisted ophthalmic forceps. *Biomedical Optics Express*, 6(2):457–472, 2015.
- [18] M. Zhou, M. Hamad, J. Weiss, A. Eslami, K. Huang, M. Maier, C. Lohmann, N. Navab, A. Knoll, and M. A. Nasser. Towards robotic eye surgery: Marker-free online hand-eye calibration using optical coherence tomography images. *IEEE Robot. Autom. Lett.*, 3(4):3944–3951, 2018.
- [19] M. Zhou, X. Hao, A. Eslami, K. Huang, C. Cai, C. Lohmann, N. Navab, A. Knoll, and M. Nasser. 6dof pose estimation for robot-assisted vitreoretinal surgery. *IEEE Access*, 7:63113–63122, 2019.
- [20] Q. Zhou, J. Park, and V. Koltun. Open3d: A modern library for 3d data processing. *arXiv:1801.09847*, 2018.